Solar Phys (2014) 289:4047–4067
DOI 10.1007/s11207-014-0564-0

Areas of Polar Coronal Holes from 1996 Through 2010

S.A. Hess Webber · N. Karna · W.D. Pesnell · M.S. Kirk

Received: 7 April 2014 / Accepted: 20 June 2014 / Published online: 4 July 2014

Abstract Polar coronal holes (PCHs) trace the magnetic variability of the Sun throughout the solar cycle. Their size and evolution have been studied as proxies for the global magnetic field. We present measurements of the PCH areas from 1996 through 2010, derived from an updated perimeter-tracing method and two synoptic-map methods. The perimeter-tracing method detects PCH boundaries along the solar limb, using full-disk images from the *SOlar and Heliospheric Observatory*/*Extreme ultraviolet Imaging Telescope* (SOHO/EIT). One synoptic-map method uses the line-of-sight magnetic field from the SOHO/*Michelson Doppler Imager* (MDI) to determine the unipolarity boundaries near the poles. The other method applies thresholding techniques to synoptic maps created from EUV image data from EIT. The results from all three methods suggest that the solar maxima and minima of the two hemispheres are out of phase. The maximum PCH area, averaged over the methods in each hemisphere, is approximately 6 % during both solar minima spanned by the data (between Solar Cycles 22/23 and 23/24). The northern PCH area began a declining trend in 2010, suggesting a downturn toward the maximum of Solar Cycle 24 in that hemisphere, while the southern hole remained large throughout 2010.

Keywords Coronal holes · Solar cycle, observations · Corona, quiet

S.A. Hess Webber · N. Karna · W.D. Pesnell (✉) · M.S. Kirk
NASA Goddard Space Flight Center, Greenbelt, MD, USA
e-mail: william.d.pesnell@nasa.gov

S.A. Hess Webber · N. Karna
George Mason University, Fairfax, VA, USA

S.A. Hess Webber
e-mail: shessweb@masonlive.gmu.edu

N. Karna
e-mail: nkarna@masonlive.gmu.edu

M.S. Kirk
NASA Postdoctoral Program Fellow, Goddard Space Flight Center, Greenbelt, MD, USA
e-mail: michael.s.kirk@nasa.gov

1. Introduction

The eleven-year solar cycle is driven by the periodic evolution of the solar magnetic field. Schatten *et al.* (1978) proposed that the polar magnetic field of the Sun could be used as a predictor of the amplitude of activity in the succeeding solar cycle. The strength of the polar field is greatest at solar minimum and appears to correlate with the amplitude of the following solar cycle (Schatten and Pesnell, 2007).

At solar minimum, the topology of the global magnetic field resembles a dipole, with regions of open field at the poles. These open-field regions correspond to large, temporally stable, polar coronal holes (PCHs, Bohlin, 1977). The open magnetic field in a coronal hole allows plasma to flow outward as the fast solar wind (Krieger, Timothy, and Roelof, 1973), meaning the coronal holes are less dense than the neighboring closed-field regions, and therefore emit less radiation than the surrounding coronal plasma. Thus, when the corona is viewed in extreme ultraviolet (EUV) or soft X-ray wavelengths, the holes appear dark compared to the closed-field corona. PCHs track the progression of the open polar magnetic field through the solar cycle as it fluctuates between the organized, quasi-dipolar field of minimum and the highly-structured field of maximum. The PCHs reach a maximum area at solar minimum and greatly diminish during solar maximum. We are interested in the evolution of growth and decay of the PCHs through the solar cycle. In particular, we wish to know whether or not the behavior of the PCH areas can be used as a proxy for the polar magnetic field, and to predict the level of future solar-cycle activity.

Waldmeier (1981) used green-line (Fe XIV 5303 Å) coronagraph data to describe the variations of the PCHs from 1940 to 1978: from before the beginning of Solar Cycle 18 until after the end of Solar Cycle 20. He concluded that the total PCH area reached a maximum of about 25 % of the solar surface during the minimum after Solar Cycle 20. Broussard *et al.* (1978) described the variation of the PCHs during Solar Cycle 20. Their Figure 4 shows that the areas covered up to 11 % in the North and 13.5 % in the South, with a small tendency to be larger in the decline of Solar Cycle 20 than in the rise. Webb, Davis, and McIntosh (1984) studied the evolution of the PCH area during and after solar maximum in Solar Cycles 20 and 21 and found that the PCH area did not reach a minimum size until about one year after solar maximum. The PCH areas during Solar Cycles 21 and 22 were examined by Bravo and Stewart (1994) using K-coronagraph data, while the green-line data were used by Dorotovič (1996) to study Solar Cycles 18 – 22. The noise in the PCH areas led Bravo and Stewart (1997) to use the total coronal hole area derived from a potential-field model as a predictor of solar activity. They concluded that the annual-average sunspot number in Solar Cycle 23 would have a maximum amplitude of 192, well above the prediction using polar-field strengths by Schatten and Pesnell (1993) and the actual value of 120. Later, Harvey and Recely (2002) tracked and identified coronal holes through drawings of He II 10 830 Å observations during Cycles 22 and 23.

More objective computational methods for coronal-hole detection and boundary tracking were developed during Solar Cycle 23 by, *inter alia*, de Toma and Arge (2005) and Malanushenko and Jones (2005). Image-analysis methods, such as morphological analysis (Henney and Harvey, 2005) and intensity and magnetic contrasting (Scholl and Habbal, 2008), were developed and used to identify coronal holes in solar images. de Toma (2011) used magnetic and intensity threshold contrasting techniques to determine the total coronal-hole area over the entire Sun. Krista and Gallagher (2009) used intensity-threshold contrasting and magnetic-skewness contrasting techniques to specifically examine equatorial coronal-hole areas in conjunction with solar-wind streams. Kirk *et al.* (2009) investigated the PCH areas, distinguishing between hemispheres, by applying morphological analysis and intensity-threshold contrasting techniques to EUV images.

Any image analysis of the polar regions of the Sun is complicated by projection effects. As the observed point moves from disk center toward the limb, it is seen through the corona at an ever-increasing angle. Coronal holes at low- to mid-latitudes will be seen at favorable viewing geometries when they rotate past the observer or by using data from another satellite near the Ecliptic plane. Polar regions of the Sun have not yet been imaged at optimal viewing angles.

The line-of-sight (LOS) view through the coronal plasma obscures the equatorward edge of a PCH as it passes the central meridian and reduces the accuracy of the measured location. Emissions at EUV wavelengths from gases with smaller scale heights allow better resolution of the PCH boundaries, but the images at hotter temperatures have better contrast between the material inside and outside the coronal hole.

We first describe the methods used to measure the variation of the PCH areas in time. Next, we extend the results of Kirk *et al.* (2009) to describe the evolution of the PCH areas through Solar Cycle 23 and the early part of Solar Cycle 24. After conclusions, some details of the analysis are discussed in the Appendix.

2. Detection Methods

We report PCH areas from three techniques. Two methods, perimeter tracing (Kirk *et al.*, 2009) and the analysis of EUV synoptic maps described here, used data from the *SOlar and Heliospheric Observatory*'s *Extreme ultraviolet Imaging Telescope* instrument (SOHO/EIT: Delaboudinière *et al.*, 1995). The third method analyzed LOS magnetic-field magnetograms from the SOHO/*Michelson Doppler Imager* (MDI: Scherrer *et al.*, 1995; Hoeksema *et al.*, 2000). All three analyses agree in the general variation of the PCH areas during Solar Cycle 23 and the initial phases of Solar Cycle 24, but disagree in the fine structure of that temporal variation.

2.1. Perimeter-Tracing Method

Perimeter tracing (PT) is a method for detecting the PCH boundary at the solar limb, first described by Kirk *et al.* (2009). In summary, the bounding latitudes of PCHs along the limb are measured and used to estimate the centroid, perimeter, and fractional area of the polar holes. The bounding latitudes are mapped out through one complete Harvey Rotation (HR: one polar rotation of 33 days). The data are then fit with a curve from which the centroid, perimeter, and area are derived. See Figures 4 and 5 in Kirk *et al.* (2009) for an overview of the methodology, as well as the top images in our Appendix Figure 12. This algorithm was used to analyze SOHO/EIT images in three EUV wavelengths: He II 304 Å, Fe XI/X 171 Å, and Fe XII 195 Å.

Several adjustments were made to the original PT algorithm. First, the EIT image dataset used in the analysis was extended through the end of 2010, after which the number of available images drops to too few per day to accurately measure the PCH areas. Next, all available EIT images were used, rather than the one image per day used by Kirk *et al.* (2009). This increase in temporal resolution reduces the effect of isolated divergent points in the χ^2 minimization fit that determines the perimeter and area of the PCH. The thresholding parameters of each wavelength were then adjusted to more accurately detect boundary points. Finally, our limiting polar-latitude boundary was changed to 50°, for consistency in comparing to other PCH area-calculation methods and polar magnetic-field data (Svalgaard, Duvall, and Scherrer, 1978; Waldmeier, 1981;

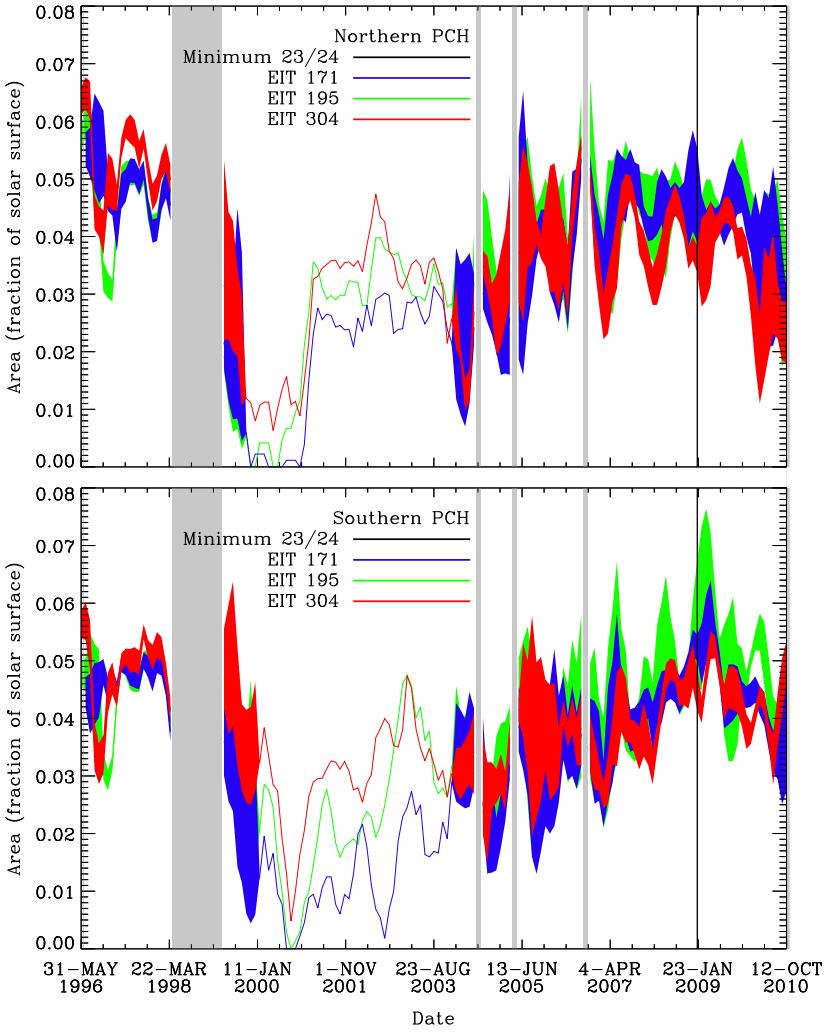

Figure 1 Perimeter-tracing fractional-area plots of the northern (top) and southern (bottom) PCH between June 1996 and October 2010 (HR 1068 – HR 1226 or CR 1911 – CR 2101), for EIT 171 Å (blue), EIT 304 Å (red), and EIT 195 Å (green). The solid-gray regions denote periods where the data were insufficient to adequately sample an HR. The vertical-black line indicates the time of the accepted Solar Minimum 23/24. The width of the lines indicates the calculated uncertainty of the least-squares fit used to determine the PCH areas (see Kirk *et al.*, 2009). Note that the uncertainty due to the annual periodicity is not included in the width, since it is not a variable of the fitting routine. The uncertainty is not shown for the solar-maximum data because false boundary detections during that time contaminate the fitted data.

Hoeksema, 1995). With these adjustments, we measured the PCH areas from mid-1996 through 2010 (Figure 1).

It is readily apparent that an annual variation is present in the PCH areas shown in Figure 1. We investigated the cause of this variation by modifying the PT method and by introducing two independent estimates of the PCH areas. Because this effect is also seen in the PCH areas derived from the EIT synoptic maps discussed below, we discuss these changes

in the Appendix. In short, the annual periodicity in the PCH area data of both EIT image analyses is caused by the variation of the solar B_0 angle, despite the fact that the PT method was designed to remove this effect. After verifying SOHO's orbital information, we investigated several simple explanations of the cause of the periodicity, and we applied new filtering techniques to the PT algorithm in an effort to remove the fluctuations. Ultimately, none of these inquiries successfully accounted for the annual fluctuations, and we conclude that the periodicity is included in the spacecraft ephemeris data. Again, see the Appendix for details.

2.2. Synoptic Map Methods

Two methods were developed using synoptic maps to measure the areas of the PCHs. Synoptic maps are constructed by concatenating strips of equal width in longitude, centered on the central-meridian longitude of each solar disk, over a 27.27 day Carrington Rotation (CR). The strips are mapped by increasing Carrington Longitude onto a rectangular grid. In Sections 2.2.1 and 2.2.2, we discuss the details of the image processing and analysis of the synoptic maps constructed from EUV images from the EIT instrument and LOS magnetic fields from the MDI instrument onboard SOHO.

2.2.1. EIT Synoptic Maps

We used synoptic maps from the SOHO/EIT archive to calculate the fractional PCH area between CR 1911 (June 1996) and CR 2055 (March 2007) (Benevolenskaya, Kosovichev, and Scherrer, 2001). The maps were built using the same wavelengths as were used in the PT method (171 Å, 195 Å, and 304 Å), discussed in Section 2.2 above. The archive's synoptic maps were constructed using longitudinal strips of 16°, centered on the central meridian, and running from latitude $-83°$ to $+83°$. They have 1° resolution in both longitude and latitude (Benevolenskaya, Kosovichev, and Scherrer, 2001).

Because the EIT synoptic-map archive ends at CR 2055, we created synoptic maps through CR 2102 (October 2010) in all three wavelengths. The solar disk images were first mapped to the heliocentric Cartesian coordinate system (Thompson, 2006). We concatenated longitudinal strips of 13.6°, centered on the central meridian and running from latitude $-90°$ to $+90°$, from four images per day over each CR. Each strip overlaps its neighbors by 3/4 of its width. The average pixel value was calculated by taking the arithmetic average of the photon counts in the overlapping pixels. Pixels with missing data were ignored during averaging and counting. The size of the constructed synoptic maps is 3600×1080 pixels ($10' \times 6'$), with longitude and latitude in degrees along the x- and y-axes, respectively. Pixel values are displayed with a logarithmic scaling that is similar to the one used in the EIT images. These maps are available on the George Mason University Space Weather website (www.spaceweather.gmu.edu).

Because coronal holes are regions of low-intensity pixels, we selected the first local minimum of the histogram of each synoptic map as an initial threshold estimate (for example, see Figure 1 of Karna, Hess Webber, and Pesnell (2014)), then we adjusted the initial value for a best visual fit of the PCH in the map. To calculate the fractional area of the northern PCH in each map, we summed over the latitudes above the polar limit ($\theta > 50°$):

$$A_{\mathrm{PCH}}^{N} = \frac{2\pi^2}{pq} \sum_{\theta > 50°} n(\theta) \cos\theta, \tag{1}$$

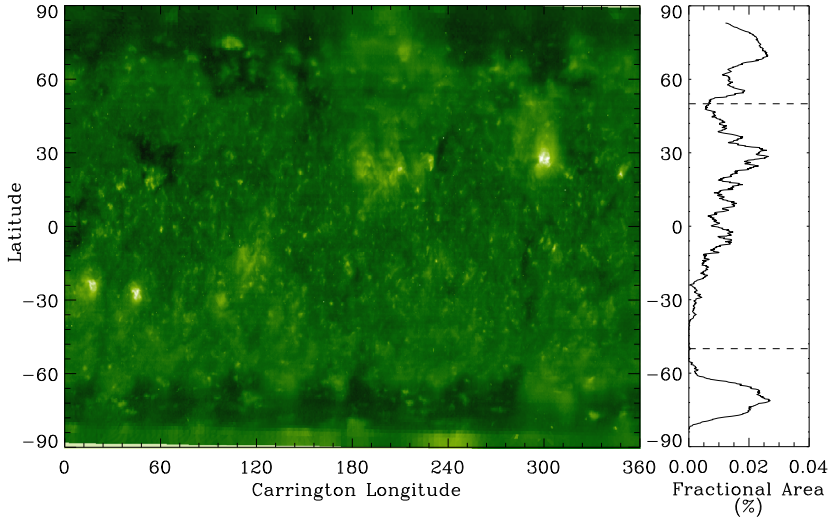

Figure 2 The left image shows an EIT 195 Å synoptic map (CR 2084) corresponding to 30 May 1999 – 26 June 2009. The lighter regions at the top and bottom of the map show the latitudes obscured by the solar B_0-angle. To the right is the corresponding plot of the longitudinally averaged fractional coronal-hole areas with respect to latitude. The dashed lines at $\pm 50^\circ$ indicate the limiting polar latitude, above which the coronal holes are considered polar features. The fractional-area peaks at either pole of the plot represent the percentage of longitudinally averaged PCH fractional areas at each latitude. The integral below the curve gives the total fractional PCH area. The fractional northern and southern PCH areas are 2.6 % and 2.2 % for this CR.

where θ is latitude, $n(\theta)$ is the total number of dark pixels at each latitude, p is the total number of pixels in latitude, and q is the total number of pixels in longitude. Similarly, the fractional area of the southern PCH was calculated from Equation (1) by instead summing over latitudes $\theta < -50^\circ$. Figure 2 shows a synoptic map for CR 2084 (June 2009) on the left and the fractional area as a function of latitude on the right. The dashed lines on the right show the cutoff latitudes of $\pm 50^\circ$.

The PCH areas derived using the EIT synoptic-map method are shown in Figure 3. The annual variation present in Figure 1 can also be seen in these PCH areas.

2.2.2. *MDI Synoptic Maps*

Magnetic-field data from the SOHO/MDI instrument (Scherrer *et al.*, 1995) were used in our second synoptic method. MDI synoptic charts were generated by the Stanford *Solar Oscillations Investigation* (SOI) team from the definitive Level 1.8 magnetograms over the course of each Carrington rotation (Liu *et al.*, 2012). These magnetograms are the calibrated two-arcsecond MDI images of the solar LOS magnetic field and were produced at a 96-minute cadence. The blue regions in the magnetogram synoptic maps (for example, see Figure 4) are regions of positive magnetic field, where the LOS magnetic field is directed toward the viewer. Red regions denote negative LOS field, where the magnetic field is directed away from the viewer. Gray areas indicate where the LOS magnetic field is close to zero. These images have a cutoff-field magnitude of $\pm$ ten gauss.

To determine the boundary of the PCH in the MDI synoptic maps, we searched for the polarity-reversal boundary. The boundary of the PCH was obtained by first averaging the LOS magnetic-field strength in longitude at each latitude. The PCH boundary is at the

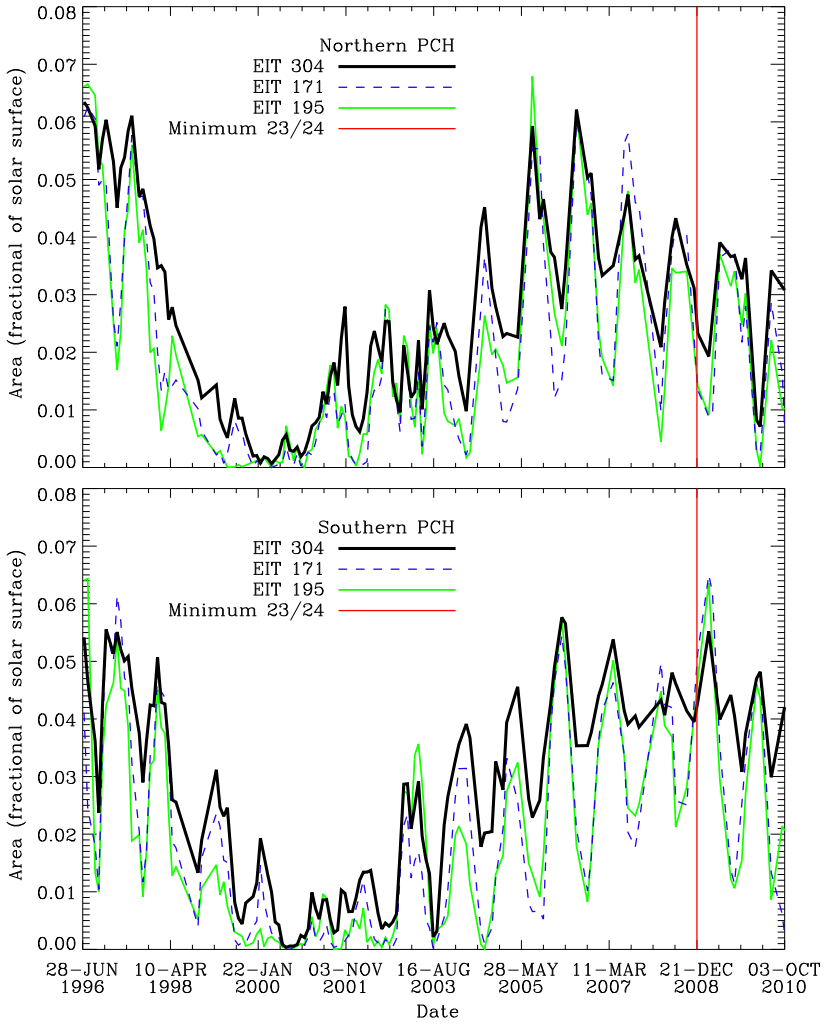

Figure 3 The northern (top) and southern (bottom) fractional PCH areas derived from the synoptic-map analysis between June 1996 and October 2010 (CR 1911 – CR 2101) for EIT 171 Å (blue), EIT 195 Å (green), and EIT 304 Å (black). The vertical-red line indicates the time of the accepted Solar Minimum 23/24.

polarity-reversal latitude [$\theta_{\rm pr}$], where the field changes sign from the dominant polarity at each pole (see Figure 4). The fractional PCH area [A] centered on the time interval spanned by the CR, is then calculated using

$$A = \frac{1}{2}\left(1 - \sin|\theta_{\rm pr}|\right). \tag{2}$$

The calculated MDI areas have temporal gaps when data are missing or when the effects of magnetic surges were removed from the data. A magnetic surge extends the apparent PCH boundary toward lower latitudes as the poleward migrating streams of magnetic flux merge into the polar regions. The stretching of the polarity boundary made locating the exact

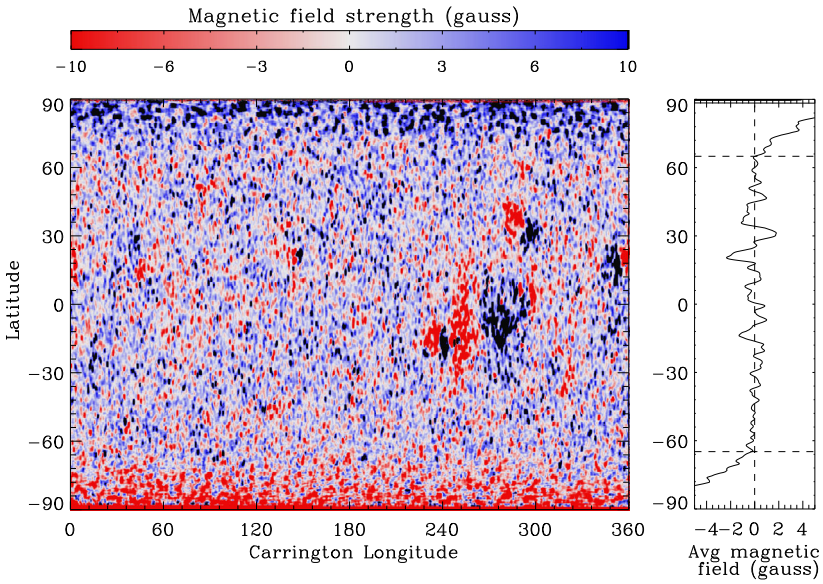

Figure 4 The left image shows an MDI synoptic map (CR 1911) corresponding to 28 June 1998 – 25 July 1998. Red regions have negative polarity and blue regions have positive polarity. To the right is the corresponding plot of the longitudinally averaged magnetic-field strength, with respect to latitude. The average-field plot demonstrates the unipolarity at the poles, from which we determine the PCH boundaries. The dashed-horizontal lines at either pole indicate the location of the PCH boundary for this CR, while the dashed-vertical line indicates an average field of zero gauss.

position of the PCH boundary difficult, and pixels containing a magnetic surge were ignored in the PCH-area time series measured with the MDI synoptic maps.

To identify which data were affected by magnetic surges, we constructed a butterfly diagram by placing the longitudinally summed synoptic maps next to each other (see Figure 5 of Karna, Hess Webber, and Pesnell (2014)). The butterfly diagram tracks regions of positive and negative magnetic-field strength through time. This shows the evolution of active regions and the polar magnetic field reversals, as well as magnetic surges toward the poles. PCH areas from CRs with magnetic-surge signatures poleward of latitudes $\pm 50^{\circ}$ were not included in the PCH analysis.

The PCH areas derived using the MDI synoptic-map method are shown in Figure 5. The results are plotted with the EIT 304 Å synoptic map results for comparison. We now compare the PCH areas from all three techniques.

3. Polar Coronal Hole Areas

Figures 1, 3, and 5 display the PCH area results from all methods for the northern and southern holes. A solar-cycle trend is observed in the area results of all three methods, with larger PCHs during solar minimum and smaller PCHs during solar maximum. An annual periodicity is seen in the EIT data. We have not been able to distinguish a clear periodic signal in the MDI data because of magnetic surges. Additional analysis was made in the PT algorithm in an effort to reduce these annual fluctuations; however, none of the studies or

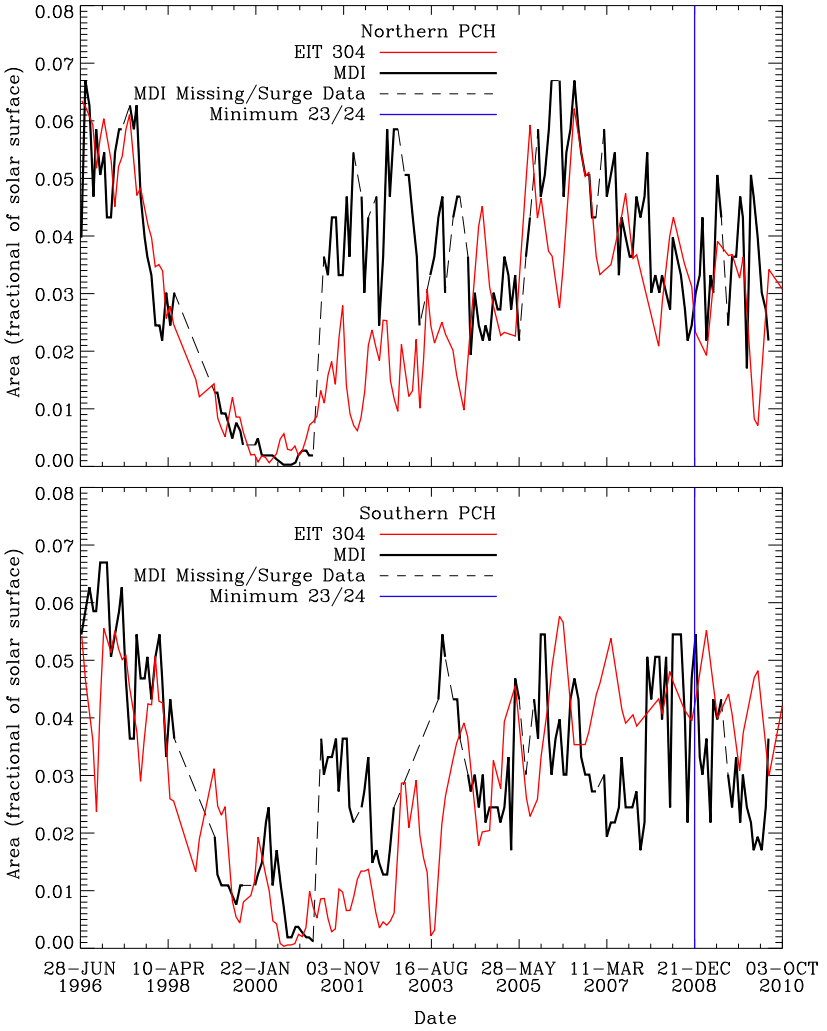

Figure 5 The northern (top) and southern (bottom) fractional PCH areas, June 1996 to October 2010 (CR 1911 – CR 2101), from the analysis of the MDI magnetograms (black), compared with EIT 304 Å (red). The dashed-black lines show periods containing missing data or when magnetic surges were removed. The vertical-blue line indicates the time of the accepted Solar Minimum 23/24.

refinements were able to fully describe or remove the periodicity. The various investigations performed are discussed in the Appendix.

During both minima, the EIT synoptic method results are consistent with the PT method results, as is demonstrated in Figure 6. The peaks of all three wavelengths tend to agree between Figures 1 and 3, although the periodic signal has a stronger effect on the two wavelengths with larger scale heights (EIT 171 Å and EIT 195 Å) in the EIT synoptic results. The uncertainty in the PT results (displayed as line thickness in Figure 1) also shows that the EIT 304 Å results are better estimates than the two hotter wavelengths. These outcomes are manifestations of the wall effect (discussed in Section A.1) in the different methods. The 304 Å emissions of the cooler He II plasma have a smaller scale height, enabling more

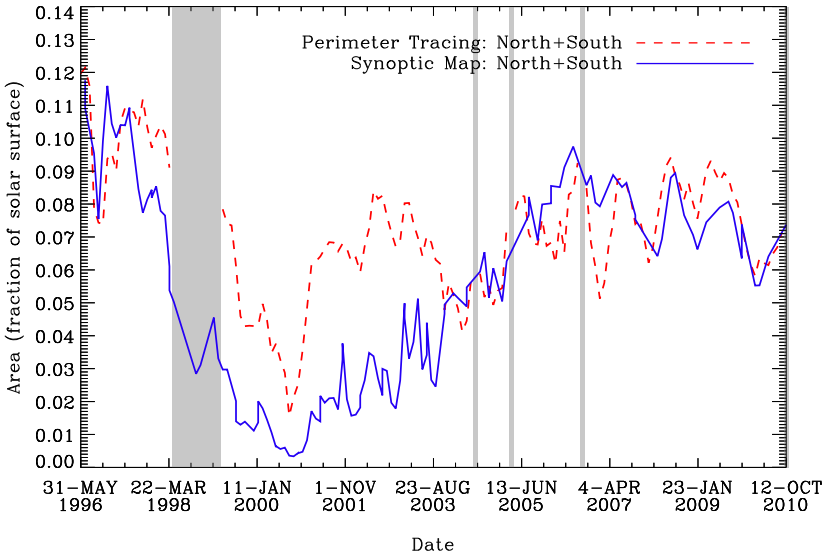

Figure 6 The two EUV methods using the EIT 304 Å image data, summed over the northern and southern PCHs. The red curve shows the sum from the PT method, while the blue curve displays the sum of the EIT synoptic-method data. The solid-gray regions denote periods where the data were insufficient to adequately sample an HR in the PT method.

precise latitude measurements in the images. For this reason, we only show the comparison of the 304 Å results in Figure 6.

The PCH areas derived from the EIT images correlate well with the areas from MDI during the times of solar minimum (see Figure 5). Around solar maximum, the magnetograms contain other magnetic features (such as magnetic surges), while the PCH boundaries can be contaminated by absorption features (such as filaments). During a surge, the whole rotation must be removed from the MDI dataset. Removing absorption features in the EIT data only requires the exclusion of a few points from the rotation in PT, while they are averaged out in the EUV synoptic maps.

3.1. Correlation Analysis

To quantitatively compare the PCH areas, we examined the correlations between the EIT and MDI synoptic data from CR 1911 (June 1996) through CR 2098 (June 2010). Data during solar maximum, CR 1958 (January 2000) through CR 2015 (April 2004), were not included because the uncertainty in the PCH areas during maximum is too large. In addition, we only used CR rotations for which both EIT and MDI data were available. The fractional areas of the northern and southern poles were added in both datasets to reduce the annual periodicity in the EIT data and improve the comparability between datasets.

The correlation coefficient [r] for each pairwise comparison was calculated as described by Taylor (1997). The fractional PCH areas of the EIT wavelengths are each plotted against those from the MDI magnetograms in Figure 7. About 70 data points were used in each of the correlations. The correlation coefficient between EIT 195 Å and MDI is approximately $r = 0.77$ and is similar for EIT 171 Å. For EIT 304 Å, $r = 0.82$. For 70 data points, these correlations are highly significant at the 99 % level (Taylor, 1997). With $r^2 = 0.59$, 0.59, and 0.67, respectively, an average 62 % of the mutual variance is explained by the correlations.

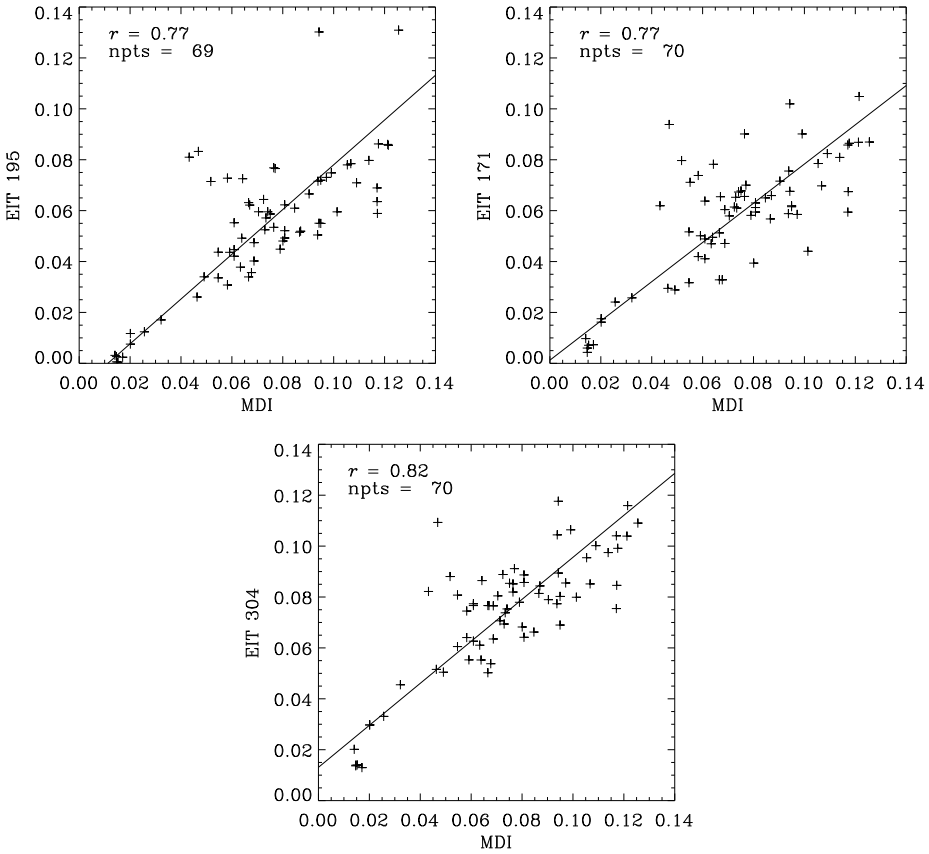

Figure 7 Correlation of the fractional PCH areas from the EIT wavelengths with the fractional area found using MDI data (top–left, EIT 195 Å; top–right, EIT 171 Å; bottom, EIT 304 Å). The correlations contain both MDI and EIT data between June 1996 and June 2010 (CR 1911 – CR 2098); however, data during solar maximum, January 2000 through April 2004 or CR 1958 – CR 2015, were not included. The northern and southern data are added to compare the total PCH area between MDI and EIT synoptic methods (this reduces the effect of the annual variation in the EIT data).

4. Results and Discussion

Through our efforts to remove the periodic signal from the EIT data (see Section A.3), we gained an important insight for interpreting the PCH areas. It is apparent that the values near the peaks of the fluctuations more accurately represent the actual PCH areas than does the running average of the complete time series. Figure 8 shows the annual peaks from the PT results. By using the peak values of the measurements, we are citing the most reliable estimates of the PCH areas that can be determined from the SOHO data.

The largest PCH areas for all three detection methods are listed in Table 1 for both hemispheres during the two observed solar-cycle minima. The area results for the two EUV methods are averaged over all three wavelengths. We also provide the average of the peak values over all three methods. These averages are the best estimate of the actual PCH areas. According to our results, the PCHs do not reach their maximum extents at the same time in both hemispheres (as can be seen in Figures 1, 3, and 5, and more clearly in Figure 8),

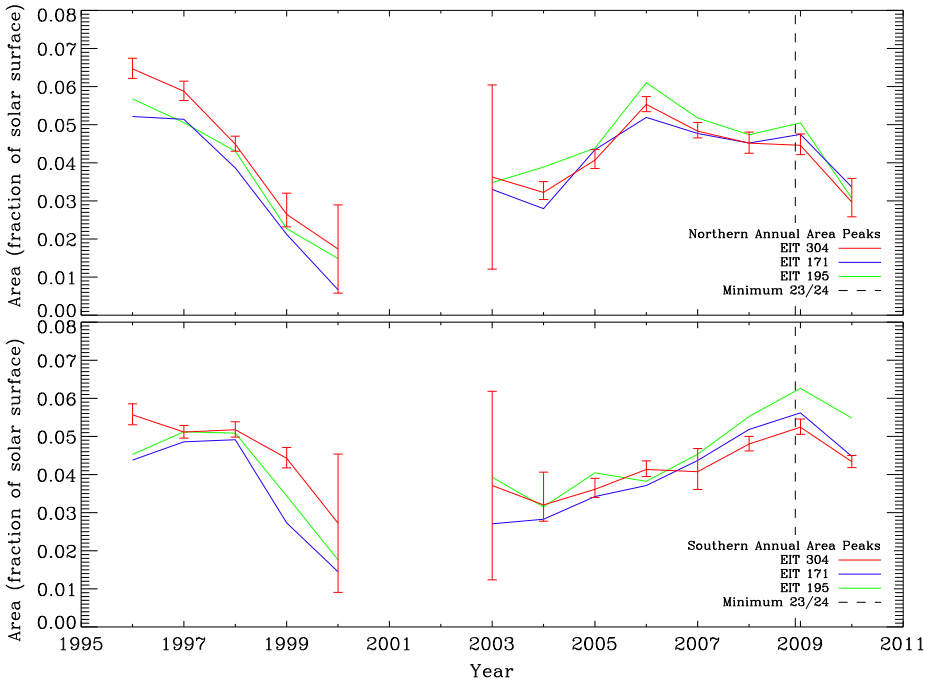

Figure 8 The annual peak PCH area values from the PT results (Figure 1), shown for the northern (top) and southern (bottom) PCH. Displayed are the PCH areas derived from EIT 171 Å (blue), EIT 304 Å (red), and EIT 195 Å (green). The vertical-black line indicates the time of the accepted Solar Minimum 23/24. The error bars show the calculated uncertainty of the least-squares fit, and are only provided for the 304 Å results because we have greater confidence in the results of that wavelength (as discussed in Section 3). Areas during the solar maximum are not shown because of the low values and large uncertainties during that time.

Table 1 Comparison of largest polar coronal hole areas.

Time of Peak	Minimum 22/23		Minimum 23/24	
	North Jun. 1996[a]	South Jun. 1996[a]	North Oct. 2005	South Jan. 2009
Perimeter tracing	6.2 %	5.5 %	5.9 %	5.8 %
EIT synoptic	6.2 %	5.7 %	5.9 %	5.9 %
MDI synoptic	6.7 %	6.4 %	6.7 %	5.4 %
Average	6.4 %	5.9 %	6.2 %	5.7 %

[a]Timing and value of these peak PCH areas do not necessarily depict the actual hemispheric area peaks during the minimum between Solar Cycles 22 and 23. The SOHO data begin in mid-1996, so the PCH in either hemisphere could have peaked earlier at a higher value.

implying that the two poles reach solar-minimum conditions at separate times. In all three methods, the northern PCH reaches its maximum area in January 2005, roughly 3.7 years earlier than the peak of the southern PCH area in October 2009. For both hemispheres, and during both solar minima, the maximum PCH areas are about 6 % of the total solar-surface area.

It is important to note that we are *not* comparing values between October 1996 and December 2008, the widely accepted dates of the respective solar minima as derived from the monthly averaged sunspot numbers. A more fundamental comparison of the solar minima would be between the maximum PCH areas in each hemisphere, as well as the time delays between the peaks of the northern and southern PCH areas within each minimum. However, the SOHO dataset does not extend far enough back in time to determine whether there was a larger PCH area in either hemisphere during the minimum between Solar Cycles 22 and 23; both hemispheres have their largest PCH area when the data begin. This also means that phasing of the peaks during that minimum cannot be determined from this data, as the hemispheres are seemingly at their highest values at the same time.

Our results indicate that there was no significant change in the maximum PCH areas between the two solar minima, while the polar-field strength saw a decline of about 50 % (Schatten and Pesnell, 2007). Therefore, the evolutionary behavior of the PCH areas does *not* appear to be a reasonable predictor of solar-cycle activity. The PCH areas prior to mid-1996 should be analyzed, using a dataset such as the Kitt Peak He I 10 830 Å or green-line corona observations, to determine when the PCH areas peaked in both hemispheres during the minimum between Solar Cycles 22 and 23 and whether there was any area decrease between minima.

The results also show that the hemispheres were out of phase during the extended minimum between Solar Cycles 23 and 24. The northern hole had already begun to shrink toward solar-maximum conditions by late 2010, whereas the southern hole had yet to show a substantial declining trend by that time (as can be seen in Figures 1, 3, and 5). This suggests that the poles will have offset polarity reversals.

An examination of other magnetic-field signatures shows that the hemispheric phase shift continues through the current Cycle 24 maximum. The "rush to the poles" method developed by Altrock (2003) suggests that solar maximum of the northern hemisphere has already occurred, while the southern hemisphere lags behind (Altrock, 2012). Similarly, Hoeksema (2012) found that the northern polar magnetic field has been weakening and predicted that the northern polarity reversal would occur in mid- to late-2012; the southern field reversal is not keeping pace. After extending this work using data from the *Solar Dynamics Observatory*'s *Atmospheric Imaging Assembly* (SDO/AIA) and SDO/*Helioseismic and Magnetic Imager* (HMI), we also conclude that the northern polar field reached solar-maximum conditions in mid-2012 and has already reversed its dominant polarity, while the southern hemisphere had not definitely gone through polar-maximum conditions by the end of 2013 (Karna, Hess Webber, and Pesnell, 2014).

5. Conclusions

We presented measurements of the polar coronal hole (PCH) areas from 1996 through 2010. We updated the perimeter-tracing method and developed methods using synoptic maps of EIT images and MDI magnetograms. Our results from these methods include the Solar Cycle 23/24 minimum period. All three methods produce comparable results. Averaged over the detection methods, both the northern and southern PCH areas reach a maximum fractional area extent of about 6 % during each solar minimum. The PCH sizes do not vary significantly between Solar Minimum 22/23 and 23/24. This makes them less appropriate as a predictor of future solar activity.

Both analyses of the EIT images produce a strong annual fluctuation in the PCH areas. The northern and southern poles are out of phase, and we determined that the periodic sig-

nal is due to projection effects introduced at the poles and limb of the solar disk (see the Appendix for details). The periodicity is included in the ephemeris data and cannot be fully removed from the PCH area calculations. The upper limit (not the average) of the PCH data most closely approximates the actual PCH areas; therefore, averaging techniques are inappropriate for smoothing the data.

Our three methods conclude that the PCH areas in the opposite hemispheres have Solar Minimum 23/24 peaks at different times, with the northern hole reaching its maximum extent in late 2005 and the southern hole in early 2009. Additionally, there is a decline in the PCH areas at the northern pole in 2010, representing a downturn toward the maximum of Solar Cycle 24. A decline is not apparent in the southern PCH area at that time.

The PCH areas from Solar Minima 22/23 and 23/24 are approximately the same. This disagrees with the polar-field strength, which is almost 50 % smaller in the later minimum.

An analysis of the variation of the PCH areas through the maximum of Solar Cycle 24 using SDO/HMI synoptic magnetograms and synoptic maps created from SDO/AIA data was reported by Karna, Hess Webber, and Pesnell (2014).

Acknowledgements This work was supported by NASA's *Solar Dynamics Observatory* (SDO). S.A. Hess Webber thanks Fredrick Bruhweiler and the Catholic University of America for their support. N. Karna thanks the Schlumberger Foundation Faculty for the Future for supporting the research. The authors thank Arthur Poland for making suggestions that improved the discussion. The EIT images are courtesy of the SOHO/EIT consortium at umbra.nascom.nasa.gov/eit/. The MDI images are provided by the *Solar Oscillations Investigation* (SOI) team of the Stanford–Lockheed Institute for Space Research. The MDI magnetic synoptic-map data and description can be accessed at soi.stanford.edu/magnetic/index6.html. SOHO is a mission of international cooperation between ESA and NASA. The MDI magnetogram data can be found at soi.stanford.edu/magnetic/index5.html. Wilcox Solar Observatory data used in this study were obtained from wso.stanford.edu/Polar.html, courtesy of J.T. Hoeksema. The Wilcox Solar Observatory is currently supported by NASA. The timing and values of solar-cycle extrema were obtained from www.ngdc.noaa.gov/stp/space-weather/solar-data/solar-indices/sunspot-numbers/cycle-data/table_cycle-dates_maximum-minimum.txt. The EIT and AIA synoptic maps constructed for use in this research can be found at spaceweather.gmu.edu/projects/synop/.

Appendix: Periodicity

PCH areas from both of the EIT image analyses have an annual periodicity in the area results, caused by the yearly variations in the B_0-angle. Additional analysis was made in the PT algorithm in an effort to reduce these fluctuations in the area results. The strongest concern regarding the periodicity was that it appeared when using the PT method, which was designed to remove the effects of B_0 from the data.

The fluctuations follow the annual variation of the B_0-angle: the pole tilted toward Earth has the larger area. A change from a polar-cap area of 5 % to 2 % (see Figures 1 and 3) implies a change in the limiting latitude from 64° to 74°. This represents almost all of the possible 14° change in B_0.

In an effort to understand the source of the periodicity, we first verified the orbital information of the SOHO spacecraft. Next, several simple explanations were investigated, but none were able to explain the variation. We also applied new filtering techniques to automate the removal of false detections from our area analysis, which we suspected were contributing to the periodicity. These filters improved the accuracy of our results, but were ultimately unsuccessful in removing the annual fluctuations.

The various investigations and filtering techniques are discussed here. We first discuss some geometric effects in the images in Section A.1 and then address a change in our working coordinate system in Section A.2. Section A.3 describes the role of the B_0-angle in

the longitudinal-coordinate calculations. Last, Section A.4 discusses the new false-detection filtering techniques that were applied to the PT analysis.

A.1 Investigation 1: Geometric Effects

A.1.1 The Wall Effect

As an equatorial coronal hole rotates into view on the limb, its leading edge is obscured by the coronal material along the LOS and then revealed as the coronal hole passes the central meridian (Timothy, Krieger, and Vaiana, 1975). We have modified their consideration of this "wall effect" for polar latitudes, including the variation in the B_0-angle, which causes an annual modulation in the measured area not seen in the equatorial case.

For polar latitudes, the wall effect can be quantified by assuming that the coronal material is a sharp edge, one scale height [H] higher than the actual solar radius [R], perpendicular to the surface of the Sun. As the solar B_0-angle increases (decreases), the LOS angle through the coronal material also increases (decreases), and H subsequently obscured more (less) to the observer. The net effect is that an external observer views a higher latitude point than the actual boundary latitude of the PCH. Adding the B_0 and wall effects, the relationship between the actual boundary latitude [θ] and the observed latitude [θ'] becomes

$$\sin\bigl(\theta' + B_0\bigr) = \frac{R}{R+H}\sin(\theta + B_0), \tag{3}$$

yielding a calculated area of

$$A = \bigl(1 - \sin\theta'\bigr)/2, \tag{4}$$

which is always smaller than the actual area of $(1 - \sin\theta)/2$.

The observed periodicity cannot be produced by the wall effect described here, where the coronal material blocks some of the area, because the limb and central-meridian sampling show the same effect. Moreover, the wall effect decreases as the area increases, while the calculations show that the amplitude increases with the area.

A.1.2 Rotation Axis

An error in the assumed position of the rotation axis at the surface of the Sun could cause the observed fluctuations in both analyses. It might also affect the determination of the longitude near the limb more than the latitude. As shown by Beck and Giles (2005), the location of the Sun's rotation axis is known well enough that this effect is too small to cause the observed fluctuations.

A.2 Investigation 2: Coordinates

We suspected that the use of the Carrington coordinate system might contribute a rotational beating effect when applied to the slower-rotating polar regions. Heliographic Carrington coordinates rotate at the mean solar rotation rate, not taking into account the differential rotation of the Sun. The heliographic Stonyhurst coordinate system is fixed with respect to the observer, while the Sun rotates beneath (Thompson, 2006). We converted the PT code to use Stonyhurst coordinates to prevent potential issues caused by rotational beating. No sig-

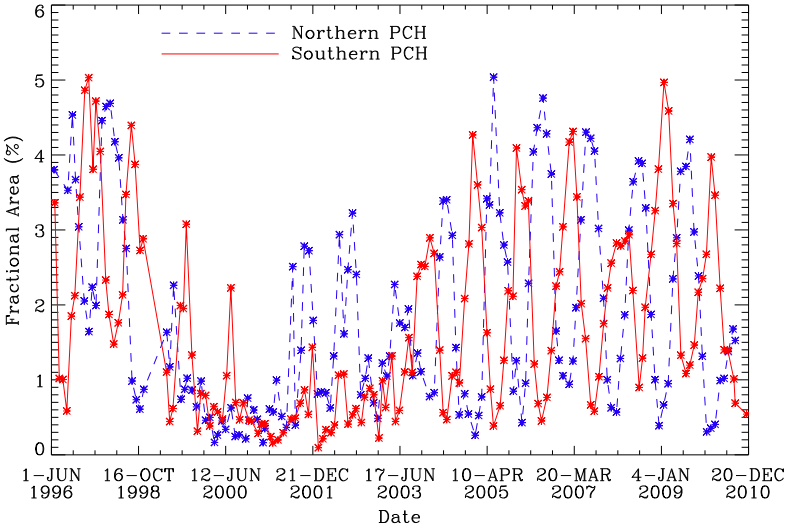

Figure 9 The areas for the northern (blue) and southern (red) PCHs, found using a simplified polar-cap calculation of the PCH boundary extent for each HR. The longitudinal coordinate inputs were found by the PT algorithm. The areas are calculated using the arithmetically averaged opening angles over each HR. This method assumes that each PCH is a polar cap.

nificant difference was detected between the Carrington coordinate system and Stonyhurst coordinate system results.

A.3 Investigation 3: Opening Angle

We also computed the PCH areas using a technique in which we found the polar position of boundary points in each image, then averaged those opening angles over each HR to determine the area. Rather than fitting the measured boundary as a polygon, this algorithm assumes the PCH is a spherical cap with the average opening angle. This approach is faster, but at the cost of a loss of accuracy in the shape of the PCH. Figure 9 shows that the annual variation from B_0 was still dominant using this simplified method when using coordinates measured from the data, despite trying to enforce its removal automatically. This confirms that the remaining B_0-variation is embedded in the images, but does not clarify how it is manifested in the results.

We expected that the B_0-angle variations would have the largest effect on our calculated latitudes, but instead found a strong annual fluctuation in our calculated longitudes, in phase with the B_0-variation, even when using Stonyhurst coordinates. The longitudinal separation of detected points fluctuated between $-180°$ and $+180°$ in an annual periodic cycle. This anomaly most likely occurred because the PCH boundaries are detected at the polar limb and the uncertainty in longitude at the limb increases as the lines of longitude converge toward the poles. Therefore, as the measured limb points approached a latitude of $\pm 90°$, the uncertainty of the measured longitude increased.

However, examining near the polar limb also helped us to understand at least part of the problem. Spherical symmetry allows us to assume that the detected limb points have a constant longitudinal separation of 180°. We assigned the Harvey Longitude of the central meridian [H_0] at the date and time of the data $\pm 90°$ to the longitudes of the eastern and west-

ern limbs, respectively. It should be noted that the H_0-parameter induces the progression of longitude in time so that the PT fits to the boundary points can still be calculated. By forcing the longitudinal points to a constant 180° difference between east and west limb points, we saw a reduction in the amplitude of the annual variation, but it also reduced the solar-cycle change in the areas, as seen in Figures 9 and 10. This confirms that the B_0-fluctuation plays an important role in determining longitude in polar regions. However, while this correction decreased the periodic amplitude, the fluctuation was not entirely removed, and it remains a significant concern.

Even so, an important insight was revealed by this investigation. Note that the northern and southern curves in Figure 10 appear to track the *peaks* (not the averages) of their corresponding curves in Figure 9. Therefore, we conclude that a running average cannot be used to smooth the data without underestimating the PCH areas. We must consider the peak area values to be the best estimates of the actual PCH areas.

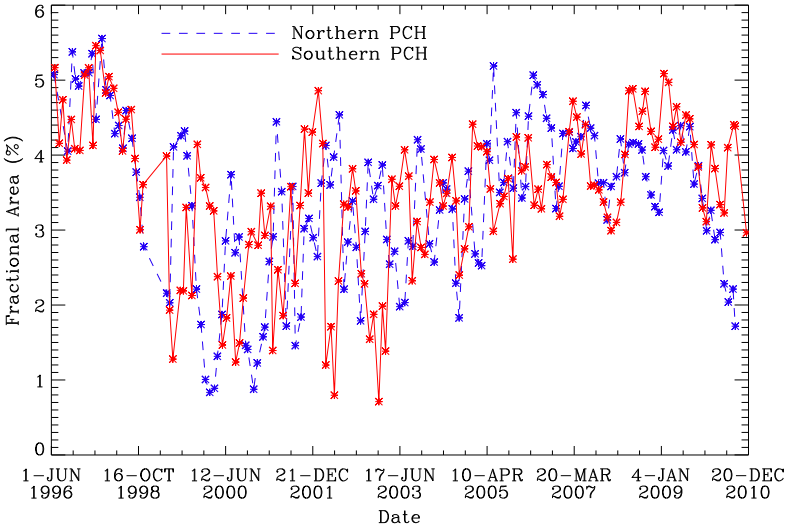

Figure 10 The polar-cap areas of Figure 9, calculated with the arithmetically averaged opening angles over each HR and with the longitudes of the data replaced by a fixed longitudinal difference. The areas have lost much of the solar cycle trend, but the prominent annual periodicity has been reduced. These areas vary in time the same as the amplitude peaks in Figure 9, suggesting that the actual PCH areas are near the upper limit of the variation.

Figure 11 Illustration of why there is a higher detection-confidence (DC) factor for a PCH enclosed between two boundary points with a large opening angle (left) than there is if the detected points are close together (right). In both images, the polar region of the solar disk is shown in dark gray, with a black rim denoting the limb where there is a detected PCH and a white rim representing the limb-brightening outside the PCH. The light-gray regions outside of the limb represent the corona at some arbitrary scale height. The black dots on the limb depict detected boundary points of the PCH. The uncertainty of whether the detected points actually bound a PCH increases as the opening angle between the points decreases. Note that for wavelengths with smaller scale heights, such as 304 Å, chromospheric phenomena can also yield similar results in the detection uncertainty (*e.g.* bright spicules on the limb).

A.4 Investigation 4: PT Filters

A.4.3 Detection Confidence

After detecting the PCH-boundary points of each wavelength, we determined the "confidence" of the detections using the ratio of the total number of PCH-pixels around the limb in either hemisphere with the total number of limb points above the limiting latitude. This detection-confidence (DC) factor is a measure of the likelihood that each detection confines a PCH. For example, if boundary points are detected close together on the limb, there must be very few potential PCH pixels in the image, and the probability that a PCH exists within

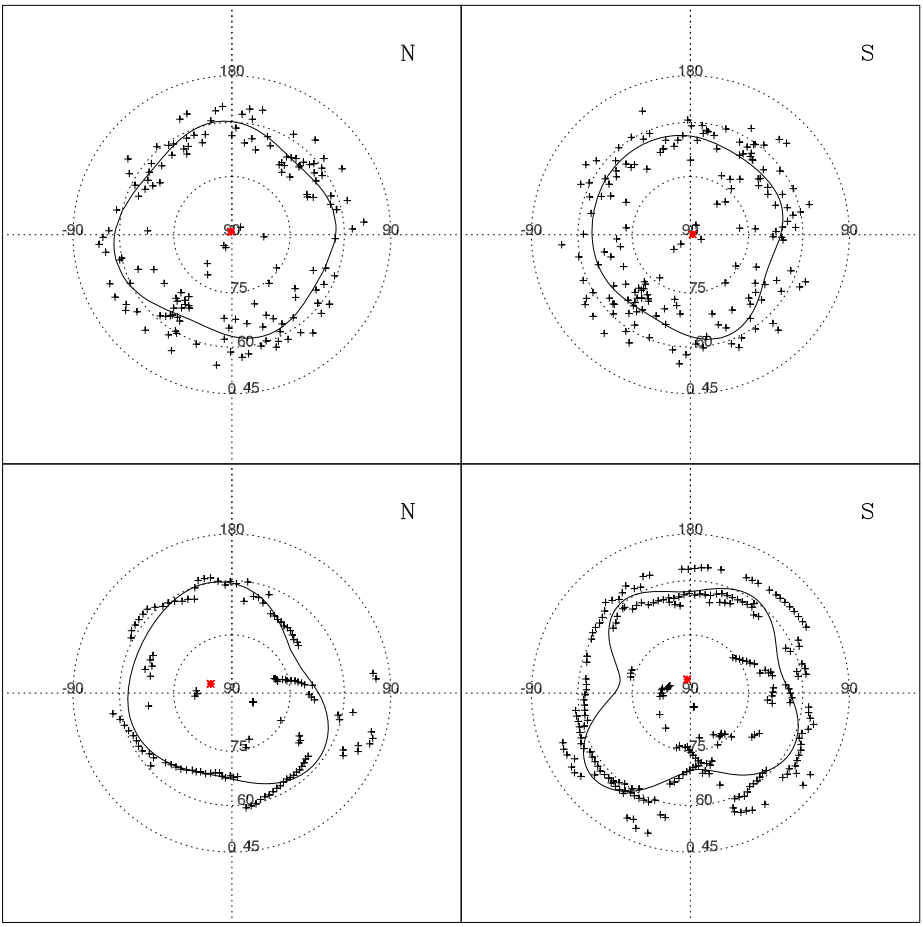

Figure 12 The northern (left) and southern (right) polar plots of the PT boundary points (+) for HR 1068 (May 1996) during solar minimum (top) and HR 1099 (March 1999) during solar maximum (bottom) of Solar Cycle 23. The solid line represents the curve of best fit from which we calculate the area of the PCH. The red asterisk (∗) is the center of the fitted curve. The detected points at minimum have a fairly uniform, circular distribution about the Pole. The best-fit line through the points is a smooth curve. During solar maximum, the detected points have a more correlated distribution, with linear features spread around the pole. These are false detections of filaments that the PT algorithm identifies as PCHs. The best-fit line is not a reasonable fit to the points. Such fits should be rejected as estimates of the PCH area.

the two boundary points is reduced (see Figure 11). A low DC factor would be associated with the boundary points in this case. The larger the DC factor, the more likely that a PCH is enclosed between the two boundary points in that hemisphere. This factor reveals nothing about the accuracy of the detections (whether the detected points are good representations of the PCH boundary points); however, the accuracy of our PT-detection technique has been verified by the results of our two synoptic methods.

We investigated the evolution of the DC factor and noticed two distinct trends. First, the B_0-fluctuations are embedded into the DC values because of the projection in the image. The DC factor is highest in either hemisphere when that pole is inclined toward Earth, as we expect from the projection effects. The B_0 trend in the DC factor is lost within the detection noise during solar maximum. Second, the DC factor also distinguishes the solar-cycle trend in its magnitude. Outside of solar maximum, the DC factors range between a maximum of 1.0 to a minimum of about 0.4. During maximum, the DC factor frequently drops well below this range. We implemented a filter that weights the fit of the detected points according to their DC factor, disregarding any points with a DC factor below the 0.4 threshold. We then eliminated rotations with too few valid coordinate-point detections from consideration.

After fitting the polar plots of each filtered HR with trigonometric fits (Kirk *et al.*, 2009), the polar fits were closed curves with improved goodness-of-fit and match the reality of the holes. The period of solar maximum was also made clear in the fitted polar plots as an unreasonably correlated distribution of the detected points. Figure 12 shows examples of the fitted polar plots for two HRs in Cycle 23, one during minimum, the other during maximum.

A.4.4 Absorption

False detections due to absorption features, such as filaments, pass through the DC and boundary-forcing filters. These features appear in the polar plots of the data as smooth curves, and are particularly prevalent during the solar-maximum period (as seen in Figure 12). To remove absorption-feature detections, an absorption-feature filter was added to

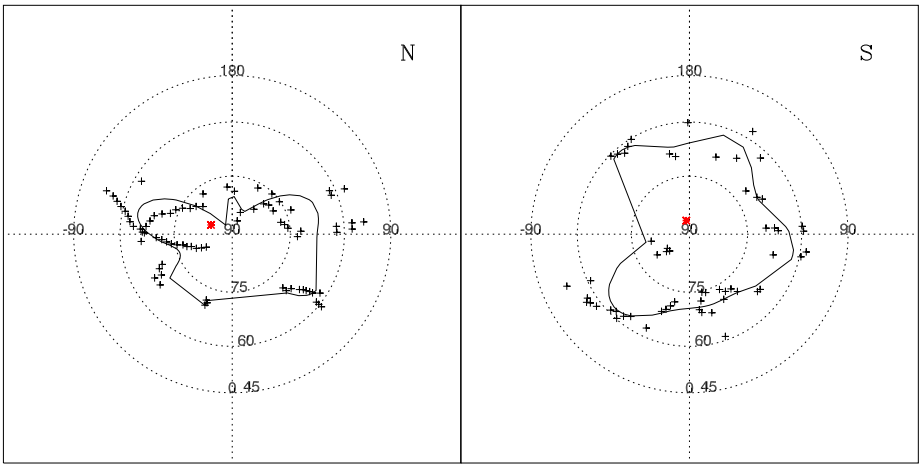

Figure 13 The northern (left) and southern (right) polar plots of the PT boundary points (+). The solid line represents the curve of best fit from which we calculate the area of the PCH. These plots show the distribution of points for HR 1099 (March 1999) during the solar maximum period of Cycle 23, after applying an absorption feature filter (compare with Figure 12). The red asterisk (∗) is the center of the fitted curve. The linear distribution of points is mainly removed and the area within the best-fit line is greatly reduced.

the algorithm, which takes advantage of the consistent curvature signature of most absorption feature data. The filter sets a lower-limit threshold on the latitudinal coordinate difference between consecutively detected points. This is effective because as a filament rotates across the limb of the solar disk, the detected latitude changes less with time than that of a PCH-boundary detection. Data with latitude differences that did not meet the threshold criteria were omitted from the fit. The data from each quadrant were treated separately.

After implementing this filter, we found that for the same solar maximum HR displayed in the bottom row of images in Figure 12, we constrain the fitted data to those shown in Figure 13, in which the "linear" false detections from absorption features are visibly reduced.

References

Altrock, R.C.: 2003, Use of ground-based coronal data to predict the date of solar-cycle maximum. *Solar Phys.* **216**, 343. ADS. DOI.

Altrock, R.C.: 2012, Cycle 24 northern-hemisphere solar maximum observed in Fe XIV. *Am. Astron. Soc. Meeting Abs.* **220**, 123.03. ADS.

Beck, J.G., Giles, P.: 2005, Helioseismic determination of the solar rotation axis. *Astrophys. J. Lett.* **621**, L153. ADS. DOI.

Benevolenskaya, E.E., Kosovichev, A.G., Scherrer, P.H.: 2001, Detection of high-latitude waves of solar coronal activity in extreme-ultraviolet data from the Solar and Heliospheric Observatory EUV imaging telescope. *Astrophys. J.* **554**, L107.

Bohlin, J.D.: 1977, Extreme-ultraviolet observations of coronal holes. I – Locations, sizes and evolution of coronal holes, June 1973 – January 1974. *Solar Phys.* **51**, 377. ADS. DOI.

Bravo, S., Stewart, G.: 1994, Evolution of polar coronal holes and sunspots during cycles 21 and 22. *Solar Phys.* **154**, 37. DOI.

Bravo, S., Stewart, G.A.: 1997, The correlation between sunspot and coronal hole cycles and a forecast of the maximum of sunspot cycle 23. *Solar Phys.* **173**, 193. DOI.

Broussard, R.M., Tousey, R., Underwood, J.H., Sheeley, N.R. Jr.: 1978, A survey of coronal holes and their solar wind associations throughout sunspot cycle 20. *Solar Phys.* **56**, 161. DOI.

de Toma, G.: 2011, Evolution of coronal holes and implications for high-speed solar wind during the minimum between cycles 23 and 24. *Solar Phys.* **274**, 195. DOI. ADS.

de Toma, G., Arge, C.N.: 2005, Multi-wavelength observations of coronal holes. In: Sankarasubramanian, K., Penn, M., Pevtsov, A. (eds.) *Large-Scale Structures and Their Role in Solar Activity* **CS-346**, Astron. Soc. Pac., San Francisco, 251.

Delaboudinière, J.-P., Artzner, G.E., Brunaud, J., Gabriel, A.H., Hochedez, J.F., Millier, F., Song, X.Y., Au, B., Dere, K.P., Howard, R.A., Kreplin, R., Michels, D.J., Moses, J.D., Defise, J.M., Jamar, C., Rochus, P., Chauvineau, J.P., Marioge, J.P., Catura, R.C., Lemen, J.R., Shing, L., Stern, R.A., Gurman, J.B., Neupert, W.M., Maucherat, A., Clette, F., Cugnon, P., van Dessel, E.L.: 1995, EIT: Extreme-ultraviolet imaging telescope for the SOHO mission. *Solar Phys.* **162**, 291. ADS. DOI.

Dorotovič, I.: 1996, Area of polar coronal holes and sunspot activity: Years 1939 – 1993. *Solar Phys.* **167**, 419. DOI.

Harvey, K.L., Recely, F.: 2002, Polar coronal holes during cycles 22 and 23. *Solar Phys.* **211**, 31.

Henney, C.J., Harvey, J.W.: 2005, Automatic coronal hole detection using He I 1083 nm spectroheliograms and photospheric magnetograms. In: Sankarasubramanian, K., Penn, M., Pevtsov, A. (eds.) *Large-Scale Structures and Their Role in Solar Activity* **CS-346**, Astron. Soc. Pac., San Francisco, 261.

Hoeksema, J.T.: 1995, The large-scale structure of the heliospheric current sheet during the ULYSSES epoch. *Space Sci. Rev.* **72**, 137.

Hoeksema, J.T.: 2012, Polar reversal, solar maximum, and the large-scale heliospheric field in solar cycle 24. *Am. Astron. Soc. Meeting Abs.* **220**, 206.07. ADS.

Hoeksema, J.T., Bush, R.I., Chu, K.-C., Liu, Y., Scherrer, P.H., Sommers, J., Zhao, X.P. (SOHO/MDI Team): 2000, Synoptic magnetic field measurements. *AAS/Solar Phys. Div. Meeting #31, Bull. Am. Astron. Soc.* **32**, 808. ADS.

Karna, N., Hess Webber, S.A., Pesnell, W.D.: 2014, Using polar coronal hole area measurements to determine the solar polar magnetic field reversal in solar cycle 24. *Solar Phys.* **289**, 3381. ADS. DOI.

Kirk, M.S., Pesnell, W.D., Young, C.A., Hess Webber, S.A.: 2009, Automated detection of EUV polar coronal holes during solar cycle 23. *Solar Phys.* **257**, 99. ADS. DOI.

Krieger, A.S., Timothy, A.F., Roelof, E.C.: 1973, A coronal hole and its identification as the source of a high velocity solar wind stream. *Solar Phys.* **29**, 505. ADS. DOI.

Krista, L.D., Gallagher, P.T.: 2009, Automated coronal hole detection using local intensity thresholding techniques. *Solar Phys.* **256**, 87. ADS. DOI.

Liu, Y., Hoeksema, J.T., Scherrer, P.H., Schou, J., Couvidat, S., Bush, R.I., Duvall, J.T.L., Hayashi, K., Sun, X., Zhao, X.: 2012, Comparison of line-of-sight magnetograms taken by the Solar Dynamics Observatory/Helioseismic and Magnetic Imager and Solar and Heliospheric Observatory/Michelson Doppler Imager. *Solar Phys.* **279**, 295. DOI.

Malanushenko, O.V., Jones, H.P.: 2005, Differentiating coronal holes from the quiet Sun by He 1083 nm imaging spectroscopy. *Solar Phys.* **226**, 3.

Schatten, K.H., Pesnell, W.D.: 1993, An early solar dynamo prediction: Cycle 23 will be similar to cycle 22. *Geophys. Res. Lett.* **20**, 2275. DOI.

Schatten, K.H., Pesnell, W.D.: 2007, Solar cycle #24 and the solar dynamo. In: Woodard, M., Stengle, T. (eds.) *Proc. 20th Inter. Symp. Space Flight Dynamics*, NASA Goddard Space Flight Center, Greenbelt 1. issfd.org/ISSFD_2007/10-1.pdf.

Schatten, K.H., Scherrer, P.H., Svalgaard, L., Wilcox, J.M.: 1978, Using dynamo theory to predict the sunspot number during solar cycle 21. *Geophys. Res. Lett.* **5**, 411. ADS.

Scherrer, P.H., Bogart, R.S., Bush, R.I., Hoeksema, J.T., Kosovichev, A.G., Schou, J., Rosenberg, W., Springer, L., Tarbell, T.D., Title, A., Wolfson, C.J., Zayer, I. (MDI Engineering Team): 1995, The solar oscillations investigation – Michelson Doppler imager. *Solar Phys.* **162**, 129. ADS. DOI.

Scholl, I.F., Habbal, S.R.: 2008, Automatic detection and classification of coronal holes and filaments based on EUV and magnetogram observations of the solar disk. *Solar Phys.* **248**, 425. ADS. DOI.

Svalgaard, L., Duvall, T.L. Jr., Scherrer, P.H.: 1978, The strength of the Sun's polar fields. *Solar Phys.* **58**, 225. ADS. DOI.

Taylor, J.R.: 1997, *An Introduction to Error Analysis: The Study of Uncertainties in Physical Measurements*, 2nd edn. University Science Books, Sausalito, 215. Chapter 9.3.

Thompson, W.T.: 2006, Coordinate systems for solar image data. *Astron. Astrophys.* **449**, 791. ADS. DOI.

Timothy, A.F., Krieger, A.S., Vaiana, G.S.: 1975, The structure and evolution of coronal holes. *Solar Phys.* **42**, 135. ADS. DOI.

Waldmeier, M.: 1981, Cyclic variations of the polar coronal hole. *Solar Phys.* **70**, 251. ADS. DOI.

Webb, D.F., Davis, J.M., McIntosh, P.S.: 1984, Observations of the reappearance of polar coronal holes and the reversal of the polar magnetic field. *Solar Phys.* **92**, 109. DOI.